Science of the Total Environment 699 (2020) 134223

Contents lists available at ScienceDirect

Science of the Total Environment

journal homepage: www.elsevier.com/locate/scitotenv

Effect of three artificial aging techniques on physicochemical properties and Pb adsorption capacities of different biochars

Lianshuai Tan [a,b], Zhanghuai Ma [a,b], Kaiqi Yang [a,b], Qingliang Cui [c,d], Ke Wang [a,b], Tongtong Wang [a,b], Gao-Lin Wu [b,c], Jiyong Zheng [a,b,*]

[a] College of Natural Resources and Environment, Northwest A & F University, Yangling 712100, China
[b] State Key Laboratory of Soil Erosion and Dryland Farming on the Loess Plateau, Institute of Soil and Water Conservation, Northwest A & F University, Yangling 712100, China
[c] State Key Laboratory of Soil Erosion and Dryland Farming on Loess Plateau, Institute of Soil and Water Conservation, Chinese Academy of Sciences and Ministry of Water Resources, Yangling, Shaanxi 712100, China
[d] University of Chinese Academy of Sciences, Beijing 100049, China

HIGHLIGHTS

- Different artificial aging techniques have different effects on SSA of biochar.
- Different artificial aging techniques lead to changes in the adsorption behavior.
- Aging increases oxygen-containing functional groups, enhancing Pb adsorption.
- Adsorption process involves complexation, van der Waals force and metal precipitation.

GRAPHICAL ABSTRACT

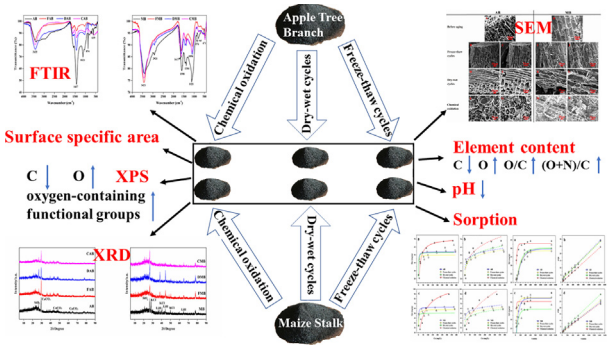

ARTICLE INFO

Article history:
Received 23 May 2019
Received in revised form 25 August 2019
Accepted 31 August 2019
Available online 02 September 2019

Editor: Baoliang Chen

Keywords:
Biochar
Physicochemical properties
Aging
Sorption experiment
Lead

ABSTRACT

Biochar is beneficial for soil amendment, but further research is still required on changes in its physicochemical properties during aging, especially in oxygen-containing functional groups and associated adsorption behaviors. Here, we used two different biochars, apple tree branch biochar and maize stalk biochar, and simulated the aging process by using freeze-thaw cycles, dry-wet cycles, and chemical oxidation methods. We investigated the changes in the physicochemical properties and Pb adsorption behavior of the biochars before and after aging treatments. The characterization results showed that the biochar surface structure changed after aging treatments. In general, the specific surface areas (SSAs) of the two biochars increased after chemical oxidation treatment but decreased after the other two treatments. The elemental content analyses indicated a decrease in the C content and increase in O content after artificial aging. In addition, the content of oxygen-containing functional groups in most biochars is increasing after treatment. The increase or decrease in SSA resulted in an increase or decrease in adsorption sites, respectively, thereby enhancing or reducing the adsorption capacity of the biochar. Furthermore, oxygen-containing functional groups enhanced the Pb adsorption capacity of biochar by complexation of free carboxyl and hydroxyl functional groups with Pb. Our research indicated that aging can lead to changes in the Pb adsorption capacity of biochar and that these changes vary depending on the type of aging and biochar. Our results will help to provide a better understanding of the changes in physicochemical properties and

* Corresponding author at: College of Natural Resources and Environment, Northwest A & F University, Yangling 712100, China.
E-mail address: zhjy@ms.iswc.ac.cn (J. Zheng).

https://doi.org/10.1016/j.scitotenv.2019.134223

Pb adsorption capacity of biochar during the aging process in soil toward making full use of biochar for soil amendment.

1. Introduction

In recent years, biochar has emerged as an environmentally functional material with great potential for application to various fields such as soil improvement, soil carbon sequestration, greenhouse effect, and pollution remediation (Guo et al., 2006; Lehmann et al., 2008; Trigo et al., 2014). Biochar refers to C-rich materials produced by heating of biomass with a limited or zero oxygen supply (Demirbas, 2004; Lehmann et al., 2006). It is not only an organic matter but also a high-quality adsorption material with abundant pores and large specific surface areas (SSAs), which have led to its wide use for increasing soil fertility and adsorption performance (Herath et al., 2013; Ahmad et al., 2014; Liu et al., 2014; Wang et al., 2018). More importantly, biochar can also react with heavy metal ions to convert heavy metals from an effective state to a residual state. Many studies have shown that biochar can not only reduce the concentration of heavy metals but also reduce their bioavailability by adsorbing them in soil and water (Uchimiya et al., 2010; Park et al., 2011; Zhang et al., 2013; Mohan et al., 2015). However, the raw materials and process parameters employed during carbonization have a great impact on the sorption capacity of biochar. Furthermore, when biochar is applied to soil, its affinity for heavy metals is also affected by environmental factors such as temperature and humidity (Chen and Yuan, 2011; Singh and Cowie, 2014; Heitkötter and Marschner, 2015). Xu and Zhao (2013) previously studied the adsorption properties of different crop straw biochars on Cu(II), Pb(II), and Cd (II) in three soils in southern China. The results showed that peanut straw biochar had better adsorption capacities than canola straw biochar. Beesley and Marmiroli (2011) found that biochar prepared by hardwood can effectively adsorb Cd and Pb in soil but cannot effectively immobilize Cu or As, which indicates that different types of biochar have specific adsorption properties for different heavy metals.

In addition, more and more studies have suggested that biochar properties may undergo long-term changes during aging due to various environmental factors (Li et al., 2016; Ren et al., 2016a; Ren et al., 2016b). The aging process will cause changes in the SSA, elemental composition, functional group content, etc. of biochar, which will affect its functionality for various applications to soil amendment, such as its ability to adsorb heavy metals. For example, Guo et al. (2014) reported that the adsorption capacity of rice husk biochar on Cu(II) decreased after aging treatment, and Mia et al. (2017b) found that the ammonium adsorption capacity of eucalyptus wood biochar increased upon chemical oxidation. Moreover, an important indicator for determining whether biochar can be successfully application in the remediation of contaminated soils is whether its strong adsorption capacity for pollutants can be maintained, especially when exposed to changing environmental conditions (Ren et al., 2018a).

At present, most studies on aging changes to the properties of biochar have been performed by using artificial methods because the aging process is very slow under natural conditions. Fan et al. (2018b) used HNO_3/H_2SO_4 and $NaOH/H_2O_2$ mixtures to oxidized wheat straw biochar and studied its adsorption behavior. Mia et al. (2017b) used different concentrations of H_2O_2 to oxidized eucalyptus wood biochar and studied its adsorption behavior for phosphate and ammonium. Liu et al. (2013) used the method of maintaining 50% water holding capacity to study the effects of aging on the properties of three biochars. Furthermore, studies have shown that these artificial methods can provide theoretical guidance for studies on biochar field aging over long periods (Mia et al., 2017a; Fan et al., 2018a). However, a single artificial aging method can only provide limited insight for the changes in the properties of biochar. Therefore, we must compare the effects of various artificial aging techniques on biochar properties to provide better theoretical guidance regarding the long-term aging process of biochar under natural conditions. In addition, biochars produced owing to different parameter (e.g., raw material, pyrolysis temperature) have different properties after the same aging treatment. Thus, the properties of different types of biochars after aging treatment, including changes in adsorption properties, also require further study.

Here, we conducted a study on apple tree branch biochar (AB) produced at 550 °C and maize stalk biochar (MB) produced at 400 °C using the three artificial aging methods of freeze-thaw cycles, dry-wet cycles, and chemical oxidation to accelerate and simulate the aging process. Among these three methods, the freeze-thaw cycles simulate the alternating recurrence process of freezing and melting of soil in the natural world due to external temperature, the dry-wet cycles simulate the process of increasing soil water content due to rainfall under natural conditions, and the chemical oxidation simulates the process that biochar undergoes changes due to biochemical oxidation reactions in the soil. We measured the physicochemical properties of the biochar samples before and after aging and performed isothermal Pb adsorption experiments on the biochar before and after aging. Our study (1) compared the effects of various artificial aging techniques on the physicochemical properties of biochars and (2) related the physicochemical properties of biochar to adsorption parameters in order to explain the change in its Pb adsorption capacity.

2. Materials and methods

2.1. Biochars

AB was provided by Shanxi Yi-xin Bioenergy company (Shanxi, China) and was produced using apple tree branches as raw materials with a high-temperature (550 °C) pyrolysis method. MB was provided by the Institute of Soil Science, Chinese Academy of Sciences (Nanjing, China) and was produced from maize stalks at 400 °C using a special carbonization furnace (China patent No. ZL200920232191.9). All the biochars were passed through a 2 mm sieve and stored in opaque sacks for further use. Soils for experiments were collected in Guyuan City, Ningxia, China. Soil's basic properties have been provided in Table S1. Stones and other impurities were removed from the soil samples before use.

2.2. Freeze-thaw cycles

The bottom 2 cm of a 7 cm diameter, 23 cm high PVC cylindrical tube was filled with quartz sand, 2–10 cm was filled with fresh soil, and 10–20 cm was filled with the biochar sample. The quartz sand and soil were separated by a glass gauze, and the soil and biochar were separated by a 0.075 mm nylon net (Fig. S1). A total of 500 mL deionized water was added to attain a moist environment, which was repeated three times. Then, the filled tube was incubated in an artificial climate box and refrigerator for cycles at 40 °C/7 d and −20 °C/7 d for 5 total cycles. After the experiment, the biochar was removed, dried, and stored in Ziplock bags for further use. AB treated by freeze-thaw cycles (FAB) and MB treated by freeze-thaw cycles (FMB) were labeled for further discussion.

2.3. Dry-wet cycles

A 30 cm long, 20 cm wide, and 12 cm high plastic box was filled with 10 cm of fresh soil. The biochar sample was fixed by a 0.075 mm nylon

net in the middle of soil. Then, the filled plastic box was incubated in an artificial climate box for five weeks, and deionized water was added once a week to achieve a 40% water holding capacity. After the experiment, the biochar was removed, dried, and stored in Ziplock bags for further use. AB treated by dry-wet cycles (DAB) and MB treated by dry-wet cycles (DMB) were labeled for further discussion.

2.4. Chemical oxidation

The biochar samples were oxidized with 15% H_2O_2 at a ratio of 1:20 (w: v) at 80 °C for 6 h in a water bath. After oxidation, the biochar slurries were dried at 105 °C in an oven to evaporate excess H_2O_2 and H_2O, then stored in Ziplock bags for further use. AB treated by chemical oxidation (CAB) and MB treated by chemical oxidation (CMB) were labeled for further discussion.

2.5. Fresh and aged biochar characterization

2.5.1. Potential of hydrogen (pH)

The pH values of the biochar samples were determined by mixing 1.00 g of each biochar sample with 20.0 mL of deionized water for 1 h in a rotary shaker. Then, the mixture was allowed to stand for 1 h at room temperature, after which the pH was measured by a PHS-3C pH meter (Rex, CHN).

2.5.2. Scanning electron microscopy (SEM)

The surface morphologies of the biochar samples were observed by a JSM-6510LV scanning electron microscope (JEOL, JPN) with a 20 kV scan voltage. All biochar samples were sputter-coated with gold before imaging to improve their conductivity and enhance the image quality.

2.5.3. Specific surface area (SSA)

Approximately 0.5 g of each biochar sample was degassed for 3 h at 125 °C, and then the SSA was determined using N_2 as the adsorbate at 77 K at a relative pressure of 0.05–0.20 with a V-Sorb 2800P SSA and pore size analyzer (GAPP, CHN). The SSAs of the biochar samples were analyzed by the Brunauer–Emmett–Teller method (Brunauer et al., 1938).

2.5.4. Fourier transform infrared (FTIR) spectroscopy

FTIR spectra were measured with the KBr pellet method. The surface functional groups of fresh and aged biochar samples were identified using a Vertex 70 Fourier transform infrared spectrometer (Bruker, USA) using 16 scans over a range of 400–4000 cm^{-1} with a resolution of 2 cm^{-1}. Method of the functional group identification were in Supplementary information.

2.5.5. X-ray diffraction (XRD) spectroscopy

The mineral species of the biochars were identified using a D/max2400 X-ray powder diffractometer (RIGAKU, USA). The biochar samples were ground as thin as possible, and the sample powder was spread evenly over the sample window. Test pieces were made by compressing the sample vertically with non-rotatable glass. The sample test pieces were prepared with flat surfaces and were placed parallel to the reference plane of the sample holder. XRD patterns were measured at a 0.02° scan step size, $2°\cdot min^{-1}$ scan speed, 0.15 mm receiving slit width, 30–40 kV accelerating voltage, and 30–40 mA of power.

2.5.6. Elemental analysis

The C, H, O, and N contents of the fresh and aged biochar were measured using a Vario EL cube elemental analyzer (German Element, GRE) with argon as the carrier gas.

2.5.7. X-ray photoelectron spectroscopy (XPS) analysis

Fresh and aged biochar samples were scanned with an ESCALAB 250 Xi X-ray photoelectron spectrometer (Thermo Scientific, USA) with a monochromatized Al Kα (1486.6 eV) source to investigate the chemical states of the main surface elements and functional groups. The experimentally obtained elemental electron binding energies were corrected to C1s (284.8 eV). In the XPS spectra, the *x*-axis indicates the binding energy, and the *y*-axis indicates the electronic counts. Method of the chemical bonds identification were in Supplementary information.

2.6. Batch sorption experiments

2.6.1. Isothermal adsorption experiments

A total of 0.10 g of each biochar sample was mixed with 50 mL of Pb $(NO_3)_2$ (initial pH 5–5.5) containing concentrations of Pb ions ranging from 50 to 500 mg/L and a background electrolyte of 0.01 mol/L $NaNO_3$. The solution was shaken in a THZ-98A thermostatic reciprocating shaker (Nanbei, CHN) at 25 °C for 1440 min. The suspension was then filtered with a 0.45 um microfiltration membrane, and the total concentration of Pb in the filtrate, which was considered as the equilibrium concentration in the solution, was determined using an ICE3500 inductively coupled plasma-atomic emission spectrometer (THERMO, USA) based on Method 6010C of USEPA SW-846. All experiments were performed in triplicate with appropriate blanks (biochar and H2O), and statistical methods were used to analyze the mean values.

2.6.2. Kinetic adsorption experiments

A total of 0.10 g of each biochar sample was mixed with 50 mL of Pb $(NO_3)_2$ (initial pH 5–5.5) containing concentrations of Pb ions of 200 mg/L and a background electrolyte of 0.01 mol/L $NaNO_3$. The solution was shaken in a THZ-98A thermostatic reciprocating shaker (Nanbei, CHN) at 25 °C for a setting period. Other conditions were the same as those used in isothermal adsorption experiments. Samples were then separated and measured.

2.7. Model fitting

2.7.1. Isothermal adsorption models

Two different models were used in this work to fit the adsorption isotherms. The equations are described as follows:

$$\text{Langmuir model}: Q_e = \frac{aQ_mC_e}{1+aC_e} \tag{1}$$

$$\text{Freundlich model}: Q_e = K_F C_e^{1/n} \tag{2}$$

where Q_e ($mg\cdot g^{-1}$) is the adsorption amount at equilibrium, Q_m ($mg\cdot g^{-1}$) is the maximum adsorption capacity, C_e ($mg\cdot L^{-1}$) is the solution concentration at adsorption equilibrium, a is the Langmuir adsorption equilibrium parameter, and K_F and n are the Freundlich adsorption parameters.

2.7.2. Kinetic adsorption models

Two different models were used in this work to fit the adsorption kinetic. The equations are described as follows:

$$\text{Pseudo-first-order kinetic model}: Qt = Qe\left(1-\exp\left(-\frac{k_1}{2.303}t\right)\right) \tag{3}$$

$$\text{Pseudo-second-order kinetic model}: \frac{t}{Q_t} = \frac{1}{k_2Q_e^2} + \frac{1}{Q_e}t \tag{4}$$

where Q_e ($mg\cdot g^{-1}$) is the adsorption amount at equilibrium, Q_t ($mg\cdot g^{-1}$) is the adsorption capacities at time (t/min), k_1 (min^{-1}) is the rate constant of pseudo-first-order adsorption, and k_2 ($g\cdot mg^{-1}\cdot min^{-1}$) is the rate constant of pseudo-second-order adsorption.

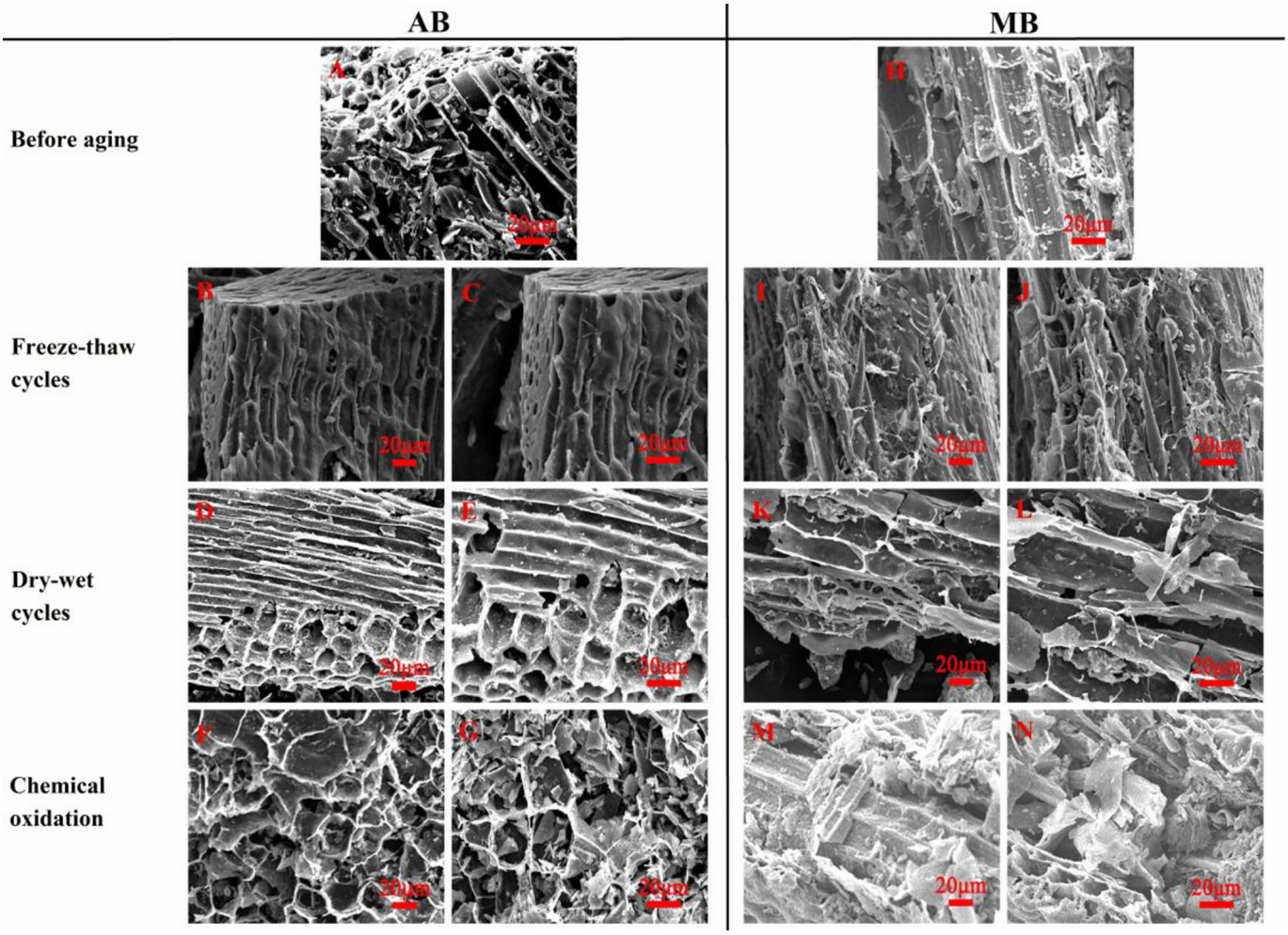

Fig. 1. Scanning electron micrographs of AB and MB before and after three different artificial aging techniques: A) AB; B–C) FAB; D–E) DAB; F–G) CAB; H) MB; I–J) FMB; K–L) DMB, and M–N) CMB.

2.8. Data analysis

The data were analyzed using SPSS v.23, and significant differences between means were determined according to *t*-test. Origin 2016 was used to fit the Langmuir and Freundlich models. In addition, XRD patterns were analyzed using Jade 6.5 to determine the mineral compositions of the fresh and aged biochars. Thermo Avantage v5.979 was used to analyze the wide XPS scans to determine the surface elemental contents and to fit the narrow C1s scans to analyze and quantify the existing C states.

3. Results

3.1. Scanning electron microscopy (SEM)

The SEM images of the two biochars are shown in Fig. 1. After freeze-thaw cycling treatment of both AB and MB, many structural pores were blocked, and the amounts of pores on the biochar surfaces showed a decreasing trend. As for the dry-wet cycled DAB and DMB, both showed rupturing of the pore structures. In addition, the rupturing of pore structures became more serious after chemical oxidation aging of MB, but a large number of small pores appeared. For AB after chemical oxidation, the micropores remained, and the pore structure became smoother and clearer.

3.2. Potential of hydrogen (pH)

The original pHs of both AB and MB showed that the biochars were alkaline substances (Table 1). After freeze-thaw aging and dry-wet aging, the pHs of both AB and MB were alkaline, and the pHs of DAB and DMB were lower than those of FAB and FMB. The pH of AB decreased from 9.79 ± 0.01 to 9.67 ± 0.02 and 9.42 ± 0.09 after freeze-thaw aging and dry-wet aging respectively, and the pH of MB decreased from 10.19 ± 0.02 to 10.12 ± 0.01 and 8.40 ± 0.19 after freeze-thaw

Table 1
pH of AB and MB before and after three different artificial aging techniques.

Treatment	Unaged	Freeze-thaw cycles	Dry-wet cycles	Chemical oxidation aging
AB	9.79 ± 0.01	9.67 ± 0.02[a]	9.42 ± 0.09[a]	5.93 ± 0.32[b]
MB	10.19 ± 0.02	10.12 ± 0.01[a]	8.40 ± 0.19[b]	4.40 ± 0.32[b]

[a] Mean the difference from the fresh biochar is significant ($p < 0.05$).
[b] Mean the difference from the fresh biochar is significant ($p < 0.01$).

Table 2
Element content (%) and SSA ($m^2\ g^{-1}$) of AB and MB before and after three different artificial aging techniques.

Type	Treatment	C	O	H	N	O/C	(O + N) / C	SSA
AB	Unaged	72.53 ± 2.24	14.85 ± 1.31	2.49 ± 0.13	1.49 ± 0.23	0.20 ± 0.02	0.23 ± 0.02	6.67 ± 0.56
	Freeze-thaw cycles	66.52 ± 1.06[a]	18.18 ± 1.20[a]	2.57 ± 0.23	1.80 ± 0.12	0.27 ± 0.02[a]	0.30 ± 0.02[b]	4.68 ± 0.60[a]
	Dry-wet cycles	67.32 ± 1.70[a]	17.84 ± 1.08[a]	2.22 ± 1.08	1.44 ± 0.11	0.27 ± 0.02[a]	0.29 ± 0.02[a]	5.58 ± 0.23[a]
	Chemical oxidation	62.69 ± 0.67[b]	21.58 ± 1.13[b]	2.86 ± 0.05[a]	1.42 ± 0.08	0.34 ± 0.02[b]	0.37 ± 0.02[b]	7.95 ± 0.48[a]
MB	Unaged	62.69 ± 3.20	14.72 ± 0.17	2.68 ± 0.15	2.27 ± 0.29	0.24 ± 0.01	0.27 ± 0.02	4.06 ± 0.22
	Freeze-thaw cycles	56.36 ± 2.08[a]	16.30 ± 0.65[a]	2.87 ± 0.10	2.12 ± 0.10	0.29 ± 0.02[a]	0.33 ± 0.02[a]	3.18 ± 0.32[a]
	Dry-wet cycles	54.81 ± 2.72[a]	16.27 ± 0.77[a]	2.92 ± 0.09	2.52 ± 0.11	0.30 ± 0.02[a]	0.34 ± 0.03[a]	3.49 ± 0.25[a]
	Chemical oxidation	55.70 ± 2.41[a]	22.83 ± 1.94[b]	2.85 ± 0.08	2.25 ± 0.19	0.41 ± 0.02[c]	0.45 ± 0.02[c]	4.76 ± 0.19[a]

[a] Mean the difference from the fresh biochar is significant ($p < 0.05$).
[b] Mean the difference from the fresh biochar is significant ($p < 0.01$).
[c] Mean the difference from the fresh biochar is significant ($p < 0.001$).

aging and dry-wet aging respectively. In contrast, the acidity/basicity of the two biochars changed markedly after chemical oxidation aging, where the pHs of AB and MB decreased from 9.79 ± 0.01 to 5.93 ± 0.32 and from 10.19 ± 0.02 to 4.40 ± 0.32, respectively.

3.3. Elemental analysis and SSA

The elemental contents and SSAs of the biochar samples are shown in Table 2. The C content of AB and MB decreased after the three different treatments, whereas the O content increased after all three treatments in both AB and MB. It is worth noting that the O content increase was significant after chemical oxidation aging for both AB and MB and was increased by 45.32% and 55.10% in AB and MB, respectively. In addition, in both AB and MB, the O:C and (O + N):C atomic ratios after the three treatments increased. The SSAs of both AB and MB decreased after freeze-thaw aging and dry-wet aging, but increased after chemical oxidation aging. For AB, the SSA decreased from 6.67 ± 0.56 $m^2 \cdot g^{-1}$ to 4.68 ± 0.60 $m^2 \cdot g^{-1}$ after freeze-thaw aging, decreased from 6.67 ± 0.56 $m^2 \cdot g^{-1}$ to 5.58 ± 0.23 $m^2 \cdot g^{-1}$ after dry-wet aging, and increased from 6.67 ± 0.56 $m^2 \cdot g^{-1}$ to 7.95 ± 0.48 $m^2 \cdot g^{-1}$ after chemical oxidation aging. Similarly, for MB, the SSA decreased by 21.67% after freeze-thaw aging, decreased by 14.04% after dry-wet aging, and increased by 17.24% after chemical oxidation aging.

3.4. FTIR

The AB, FAB, DAB, and CAB samples all contained the following FTIR peaks (Fig. 2): 3435 cm^{-1} (stretching of hydroxyl O—H), 1437 cm^{-1} (aromatic C=C stretching, indicative of lignin), and 874 cm^{-1} (out-of-plane bending of aromatic C—H). Additionally, the peaks at 1121 cm^{-1}, which represents the C—O—C stretching vibrations in cellulose and hemicellulose, and at 619 cm^{-1}, which represents the out-of-plane bending of carbonate or alkyl groups, in AB disappeared after each of the three different aging treatments.

The FTIR data showed that the peak positions and intensities in the MB, FMB, DMB, and CMB spectra were roughly similar. The spectra of the four samples contained the following peaks (Fig. 2): 3421 cm^{-1} (stretching of hydroxyl O—H), 2921 cm^{-1} (stretching of aliphatic C—H), 1384 cm^{-1} (aromatic C—C stretching), 874 cm^{-1} (out-of-plane bending of aromatic ring), and 471 cm^{-1} (Si-O-Si vibrations). It

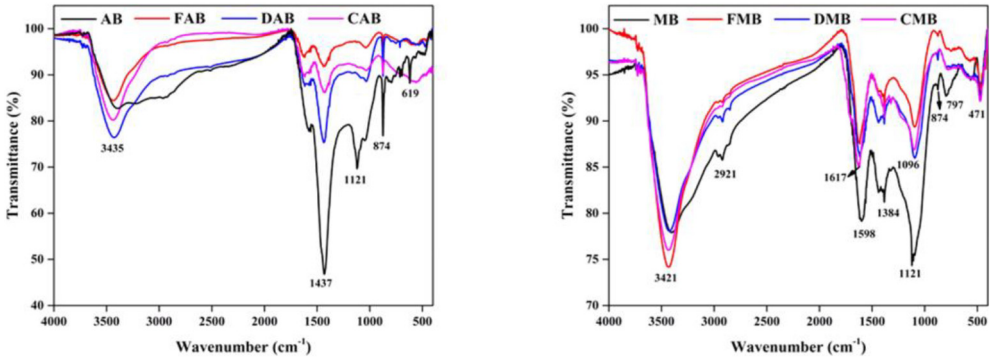

Fig. 2. FTIR spectroscopy of AB and MB before and after three different artificial aging techniques.

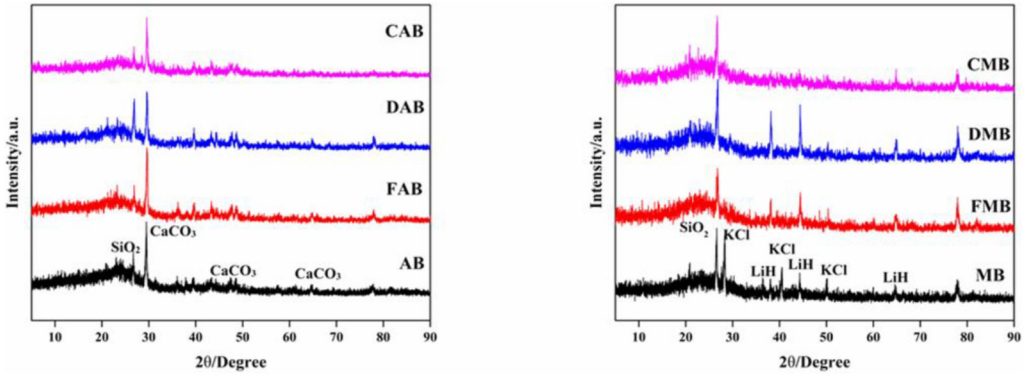

Fig. 3. XRD patterns of AB and MB before and after three different artificial aging techniques.

Table 3
Surface element composition and its relative percentage (%) on biochar samples as determined by XPS.

Type	Treatment	C	O	N	Si	Ca	O/C	(O + N) / C
AB	Unaged	86.50	10.59	1.80	1.00	0.11	0.12	0.14
	Freeze-thaw cycles	73.03	13.58	3.56	1.65	1.34	0.19	0.23
	Dry-wet cycles	77.89	17.33	3.38	1.19	0.21	0.22	0.27
	Chemical oxidation	71.26	23.32	1.21	1.27	2.94	0.33	0.34
MB	Unaged	78.67	16.86	1.22	3.25	–	0.21	0.23
	Freeze-thaw cycles	73.84	18.51	4.47	3.18	–	0.25	0.31
	Dry-wet cycles	74.49	18.04	4.33	3.14	–	0.24	0.30
	Chemical oxidation	70.84	23.60	2.03	3.53	–	0.33	0.36

"–" cannot be detected.

is worth noting that the MB peak at 1598 cm^{-1} (aromatic C═C stretching) shifted to 1617 cm^{-1} (C═O anti-symmetric stretching) after chemical oxidation treatment, and the peak at 1121 cm^{-1} (C—O—C stretching vibrations in cellulose and hemicellulose) shifted to 1096 cm^{-1} (stretching of aliphatic ether R-O-R) after all three treatments. Additionally, the MB peak at 797 cm^{-1} (aromatic ring C—H wagging) had a much higher transmittance compared to three treatments.

3.5. XRD

The XRD patterns of both AB and MB groups showed several peaks (Fig. 3), indicating the presence of mineral crystals according to related literature (Zama et al., 2018) and JADE 6.5 PDF cards. In the XRD patterns of the AB group, all four samples showed two strong peaks at 26.6° and 29.5°, suggesting that SiO_2 and $CaCO_3$, respectively, were present in AB, FAB, DAB, and CAB. The XRD pattern of MB also showed strong

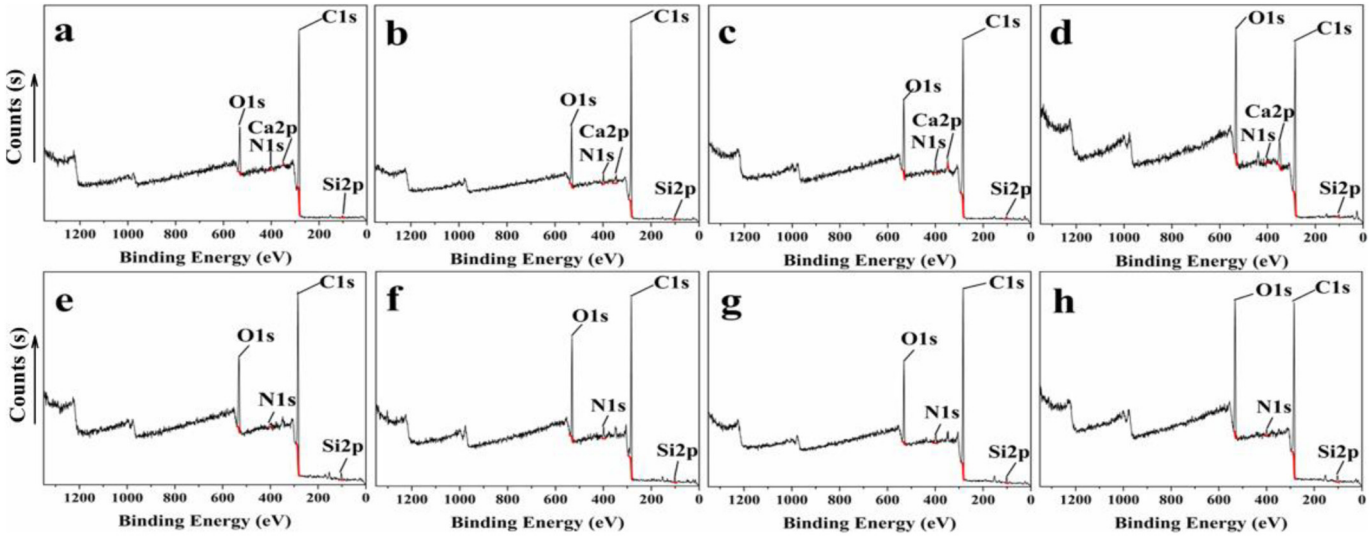

Fig. 4. X-ray photoelectron spectra (XPS) for typical survey scan of AB (a), FAB (b), DAB (c), CAB (d), MB (e), FMB (f), DMB (g), CMB (h). The black and red lines represent biochar samples and background, respectively. (For interpretation of the references to color in this figure legend, the reader is referred to the web version of this article.)

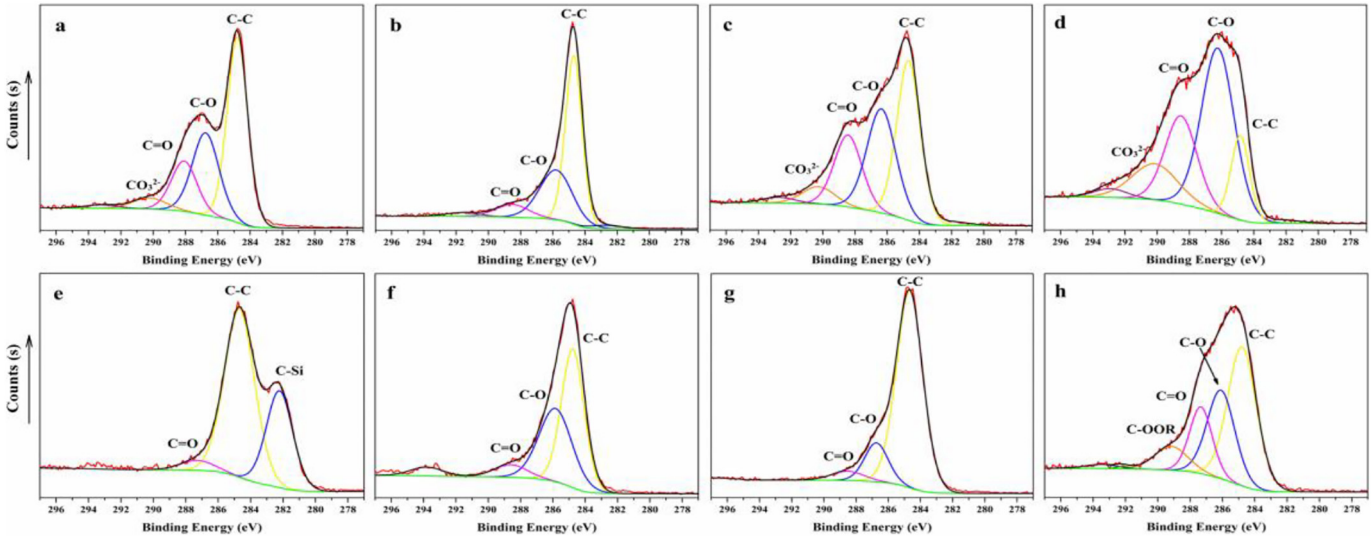

Fig. 5. XPS analysis of the C1s binding energy of AB (a), FAB (b), DAB (c), CAB (d), MB (e), FMB (f), DMB (g), CMB (h).

Table 4
The C1s bonding state and its relative percentage (%) on the biochar samples as determined by XPS.

Type	Treatment	C—Si	C—C	C—O	C═O	C—OOR	CO_3^{2-}
AB	Unaged	–	48.86	28.24	16.67	–	4.76
	Freeze-thaw cycles	–	55.05	32.04	8.23	–	–
	Dry-wet cycles	–	38.96	31.39	20.58	–	5.89
	Chemical oxidation	–	13.04	45.77	23.80	–	14.03
MB	Unaged	32.19	63.63	4.18	–	–	–
	Freeze-thaw cycles	–	62.37	28.25	1.53	–	–
	Dry-wet cycles	–	80.98	14.26	4.76	–	–
	Chemical oxidation	–	45.63	28.10	17.22	9.05	–

"–" cannot be detected.

peaks that suggested the presence of SiO_2, KCl, and LiH on the MB surface. However, after all three treatments, the KCl peaks disappeared, and after chemical oxidation, LiH disappeared. Thus, LiH and SiO_2 remained in FMB and DMB, and only SiO_2 remained in CMB.

3.6. XPS

The XPS results indicated that there were five main elements (C, O, N, Si, and Ca) on the surfaces of AB, FAB, DAB, and CAB (Table 3, Fig. 4) and only four main elements (C, O, N, and Si) on the surfaces of MB, FMB, DMB, and CMB. In addition, the C content in AB was 86.50%, which was reduced to 73.03%, 77.89%, and 71.26% in FAB, DAB, and CAB, respectively. The C content in MB also showed the same change after the three treatments, where the content was 78.67% in MB and decreased to 73.84%, 74.49%, and 70.84 in FMB, DMB, and CMB, respectively. However, the O content and O:C and (O + N):C atomic ratios of all biochar samples increased upon treatment. Furthermore, Si was detected in all biochar samples, but the original and three treated MB samples had higher Si contents than the original and three treated AB samples.

The XPS C1s core level spectra with envelope peak fitting of the biochar samples are presented in Fig. 5, and the relative concentrations of chemical bonds are shown in Table 4. The results showed that the C—C content decreased from 48.86% to 38.96% and 13.04% in AB after dry-wet cycles and chemical oxidation, respectively, and increased from 48.86% to 55.05% after freeze-thaw cycles. In addition, the C—C content decreased from 63.63% to 62.37% and 45.63% in MB after freeze-thaw cycles and chemical oxidation, respectively, and increased from 63.63% to 80.98% after dry-wet cycles. We also detected C—Si bonds in MB at a content a 32.19%, which was relatively high compared with the contents of the various other detected chemical bonds. Interestingly, we could not detect the C—Si bonds after all three different treatments of MB. In terms of the O-containing functional groups C—O, C═O, and C—OOR in AB, their contents increased after dry-wet cycles and chemical oxidation and decreased slightly after freeze-thaw cycles. Moreover, the content of C—O in MB increased from 4.18% to 28.25%, 14.26%, and 28.10% after freeze-thaw cycles, dry-wet cycles, and chemical oxidation, respectively. Furthermore, we detected C═O after all three treatments of MB, which was not detected in the original MB, and C—OOR was only detected in CMB with a content of 9.05%.

3.7. Batch sorption experiments

3.7.1. Isothermal adsorption experiments

The Pb adsorption isotherms on AB and MB before and after the three different artificial aging treatments are shown in Fig. 6. In the initial stage of adsorption, the adsorption capacity of all biochar samples increased quickly with an increase in Pb concentration until a saturation point was reached, after which the adsorption capacities tended to stabilize or rise slowly. Data fitting was performed using the Freundlich

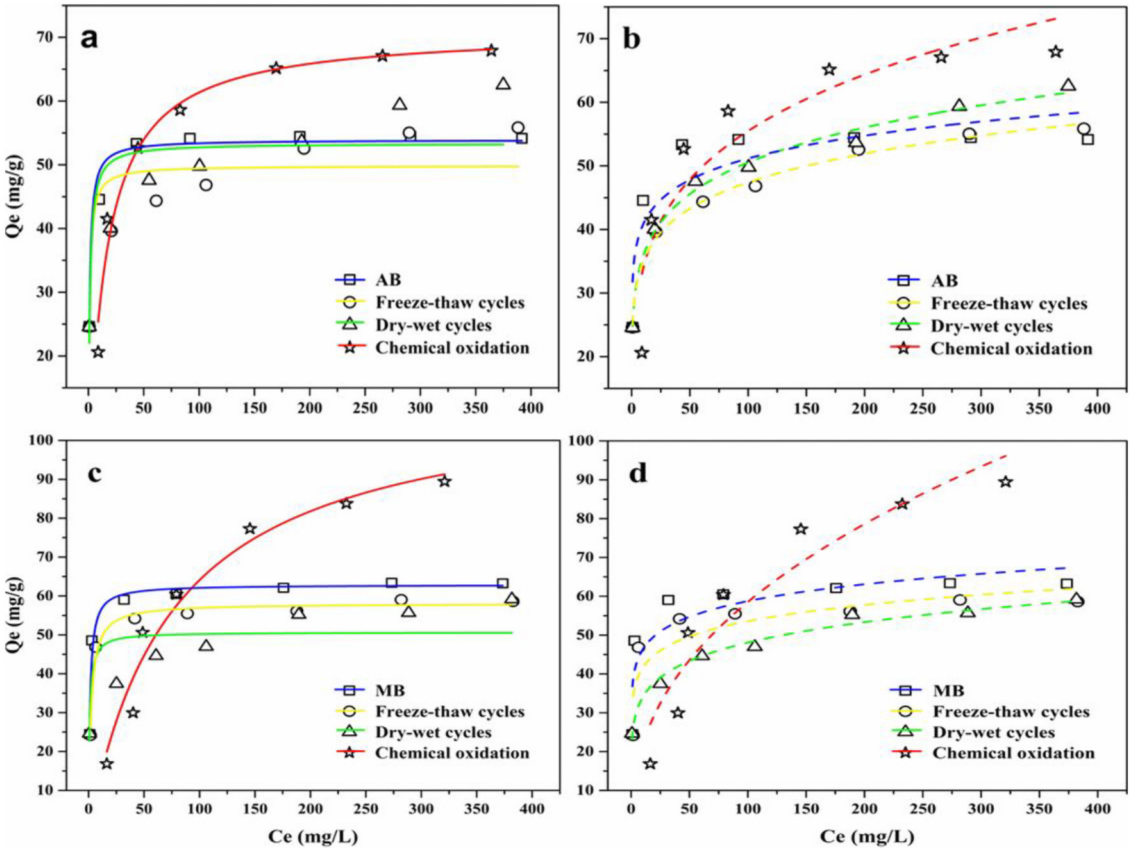

Fig. 6. Sorption isotherms of Pb on AB and MB before and after three different artificial aging techniques. Solid line (a, c) represents the Langmuir model fitting curve and dash line (b, d) represents the Freundlich model fitting curve.

Table 5
Fitting parameters of Langmuir and Freundlich isotherms for Pb adsorption by AB and MB before and after three different artificial aging techniques.

Type	Treatment	Langmuir model			Freundlich model		
		Q_m ($mg \cdot g^{-1}$)	a	R^2	K_f	n	R^2
AB	Unaged	53.903	0.996	0.9688	32.622	10.231	0.8122
	Freeze-thaw cycles	49.850	1.085	0.7613	25.909	7.622	0.9947
	Dry-wet cycles	53.353	0.842	0.7270	25.474	6.722	0.9919
	Chemical oxidation	71.071	0.063	0.9738	20.746	7.680	0.8496
MB	Unaged	62.857	0.786	0.9615	36.572	9.715	0.7610
	Freeze-thaw cycles	58.068	0.483	0.9775	32.400	9.161	0.7753
	Dry-wet cycles	50.659	1.058	0.6660	24.136	6.682	0.9853
	Chemical oxidation	113.034	0.013	0.9656	8.243	2.350	0.9056

and Langmuir isothermal adsorption models, and the fitting curves and related parameters are shown in Fig. 6 and Table 5. Among the biochar samples, only the data from FAB, DAB, and DMB had higher R^2 fits with the Freundlich model, where the other biochar samples had higher R^2 fits with the Langmuir model. For AB, the Q_m in the Langmuir model, which represents the maximum adsorption capacity, trended increased from 53.903 $mg \cdot g^{-1}$ to 71.071 $mg \cdot g^{-1}$ in CAB. In addition, trend of Q_m in MB showed decreased from 62.857 $mg \cdot g^{-1}$ to 58.068 $mg \cdot g^{-1}$ in FMB and increased to 113.034 $mg \cdot g^{-1}$ in CMB. We further calculated the dimensionless constant separation factor R_L of the adsorption reactions by the Langmuir model, which is defined as $R_L = 1/(1 + a \times C_0)$, where C_0 is the initial concentration of the solution (Mohan et al., 2007), and indicates the affinity of the adsorbent for the adsorbate. When $0 < R_L < 1$, adsorption is favorable; when $R_L > 1$, it is unfavorable; when $R_L = 1$, adsorption is linear; and when $R_L < 0$, adsorption is irreversible (Langmuir, 1916; Zhao et al., 2010). Calculated from the a values in Table 5 and C_0 values in the range of 50–500 mg/L, the R_L of AB is 0.002–0.020, CAB is 0.031–0.241, MB is 0.003–0.025, FMB is 0.004–0.040, and CMB is 0.133–0.606. All values of R_L were between 0 and 1, indicating favorable Pb adsorption. In the Freundlich model, adsorption is considered to be favorable when the n value is between 2 and 10, and K_F is related to the adsorption capacity of the adsorbent, where a larger K_F indicates a higher adsorption capacity (Freundlich, 1906; Zhao et al., 2010). As can be seen from Table 5, the n values of FAB, DAB, and DMB were between 2 and 10, indicating favorable adsorption, and the K_F values between FAB, DAB, and DMB were not very different.

3.7.2. Kinetic adsorption experiments

The Pb adsorption isotherms on AB and MB before and after the three different artificial aging treatments are shown in Fig. 7. Data fitting was performed using the pseudo-second-order and pseudo-second-order models, and the fitting curves and related parameters are shown in Fig. 7 and Table 6. Among them, the adsorption quantity of CAB increased rapidly at the beginning of the sorption experiment and about 60% of the saturated adsorption quantity was reached in 30 min. Adsorption of FAB and DAB were relatively slow, and the amount of adsorption increased gradually with adsorption time for 360 min, and

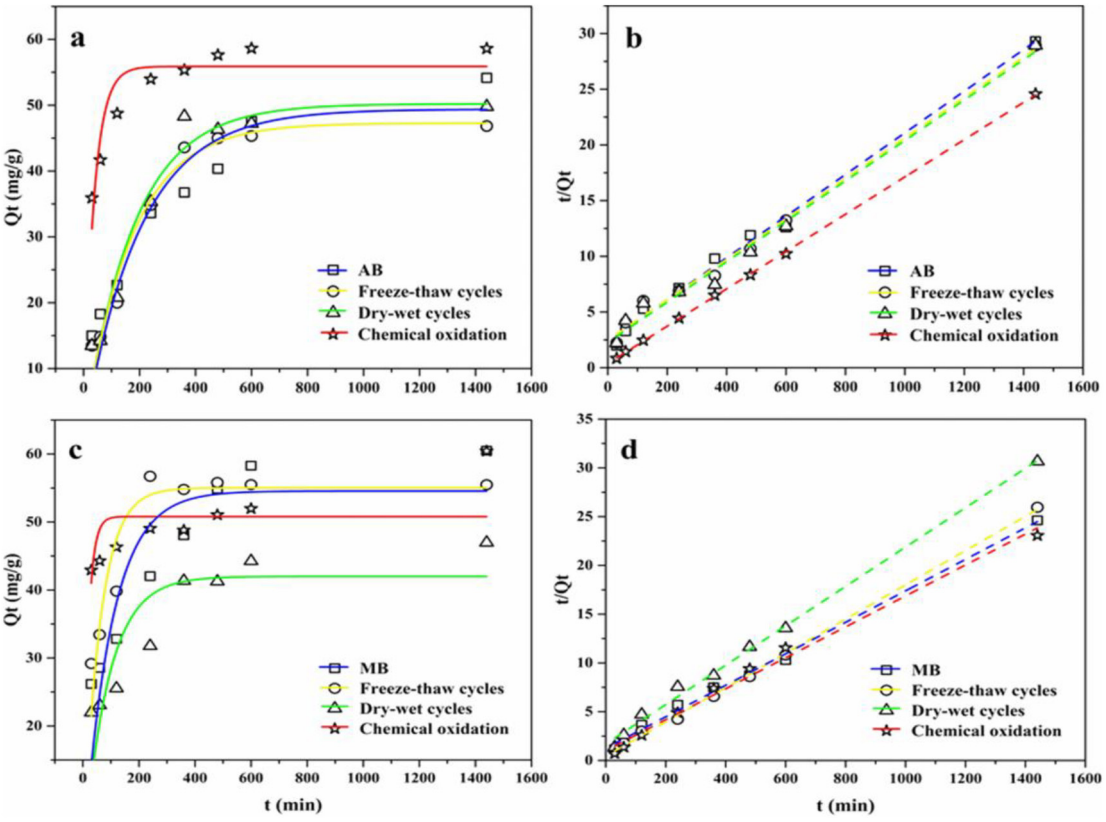

Fig. 7. Sorption kinetics of Pb on AB and MB before and after three different artificial aging techniques. Solid line (a, c) represents the Pseudo-first-order model fitting curve and dash line (b, d) represents the Pseudo-second-order model fitting curve.

Table 6
Fitting parameters of Pseudo-first-order and Pseudo-second-order kinetics for Pb adsorption by AB and MB before and after three different artificial aging techniques.

Type	Treatment	Pseudo-first-order kinetic model			Pseudo-second-order kinetic model		
		Q_e (mg·g^{-1})	k_1	R^2	Q_e (mg·g^{-1})	k_2	R^2
AB	Unaged	49.380	0.011	0.8826	53.473	0.0002	0.9939
	Freeze-thaw cycles	47.268	0.013	0.9626	55.09	0.0001	0.9927
	Dry-wet cycles	50.198	0.013	0.9578	55.126	0.0002	0.9887
	Chemical oxidation	55.873	0.063	0.8419	59.714	0.0007	0.9998
MB	Unaged	54.541	0.023	0.7515	61.955	0.0002	0.9959
	Freeze-thaw cycles	55.018	0.038	0.8632	56.937	0.0007	0.9985
	Dry-wet cycles	41.989	0.026	0.6925	49.542	0.0002	0.9958
	Chemical oxidation	50.794	0.126	0.3027	63.062	0.0002	0.9883

reached adsorption equilibrium at 720 min. In terms of the adsorption curve model fitting, from the perspective of R^2, AB and its three treated biochars were better fitted with the pseudo-second-order kinetic model. The adsorption quantity of CMB increased rapidly at the beginning of the sorption experiment and about 70% of the saturated adsorption quantity was reached in 30 min. Adsorption of FMB and DMB were relatively slow, and the amount of adsorption increased gradually for 360 min, at which point it reached adsorption equilibrium. From the correlation coefficient (R^2), MB and its three treated biochar were better fitted using the pseudo-second-order kinetic model.

4. Discussions

4.1. Changes in biochar properties with aging

Biochar is generally considered to have a large SSA and a rich porous structure. In our study, the SSA of AB increased by 19.19% after chemical oxidation, whereas it decreased by 29.84% and 16.34% after freeze-thaw cycles and dry-wet cycles, respectively. The SSAs of MB also showed the same trend, increasing by 17.24% after chemical oxidation and decreasing by 21.67% and 14.04% after freeze-thaw cycles and dry-wet cycles, respectively. The changes in the SSAs of AB and MB were supported by the SEM results. The main reason for the reduction in biochar SSA was the destruction and blockage of pore structures. When biochar is applied to soil, solid particles or plant roots in the soil can destroy its pore structure (Mia et al., 2017a), and the pore spaces can also be filled with soil organic matter (Martin et al., 2012). In addition, during freeze-thaw cycles, the dissolution and reprecipitation of inorganic minerals has been shown to often be an important cause of pore blockage (Hale et al., 2011). On the other hand, the causes of increases in biochar SSA were as follows: 1) the reduction of impurities led the pore structures became smoother and 2) formation of new pore structures. For the chemical oxidation treatment of AB, we suggest that the water bath heating process washed away the particulate impurities in the pore structures of the biochar surface and retains the microporous structure (Qian et al., 2015). For the chemical oxidation treatment of MB, even if the surface structures were severely deformed, the pore structures formed by the aggregation of aged biochar and biochar-derived organic matter still raised the SSA (Mia et al., 2017b). The same conclusion was reported by Mia et al. (2017a), who found that the SSA of biochar increased after H_2O_2 oxidation. However, Ghaffar et al. (2015) reported that the SSA decreased due to pore destruction after oxidation with an HNO_3/H_2SO_4 mixture (1:3, v/v). This may be due to the different oxidizing properties of the oxidants. Excessive oxidizing properties can cause more severe pore destruction and lead to a decrease in SSA. As there have been limited studies on SSA changes with different oxidants, the reasons for the observed SSA changes require further research.

Biochar will have different surface crystal structures based on the raw materials used in the production process. Biochar will also leach out as dissolved organic matter in the process of aging, thus affecting the biochar adsorption performance (Ren et al., 2018b). In our study, $CaCO_3$ and SiO_2 were detected on the surface of AB, and SiO_2, KCl, and LiH were detected on the surface of MB. Due to the different properties of these crystalline compounds, KCl, which is highly soluble in water, disappeared after all three treatments. As for the disappearance of LiH after chemical oxidation, we speculated that the aqueous solution environment of the treatment caused full contact and reaction of LiH with water and thus the formation of corrosive LiOH and hydrogen. Apart from this, $CaCO_3$ and SiO_2 remained in AB and MB after all three different treatments. It is worth noting that both $CaCO_3$ and SiO_2 are insoluble or poorly soluble in water and do not react with the H_2O_2 used in the chemical oxidation treatment. Therefore, we suggested that the properties of the surface crystal structures of the biochar mainly determined whether the species remained after the aging process, and changes in physical factors did not have a significant impact on their presence.

The elemental content of biochar will change under aging treatment due to oxidation and other reasons. In this study, for both AB and MB, the biochar C content decreased after the three kinds of aging treatment and the O content increased. The changes in C and O contents were due to the fact that biochar can be oxidized to form a humic substance, and O adsorbed to the biochar surface by forming functional groups (Cheng et al., 2006; Mia et al., 2017a). Additionally, the O:C atomic ratios, which were used as an index for oxidation state (Mia et al., 2017a), showed an increasing trend after the three aging treatments. This indicated that the aged biochar had a greater level of oxidation. Our results agree with those of previous studies, which showed that after natural and artificial aging, the C content decreased and O content and O:C atomic ratios increased in biochar (Cheng et al., 2006; Cheng and Lehmann, 2009; Sorrenti et al., 2016; Fan et al., 2018b). Furthermore, some studies have indicated that oxidation is a surface process (Sorrenti et al., 2016; Wang et al., 2017), and Cheng et al. (2006) suggested that oxidation begins at the biochar surface. Our XPS analyses of surface elemental compositions showed that on both the AB and MB surfaces, the C content decreased and O content and O:C atomic ratios increased after each of the three treatments, indicating that oxidation occurred on the biochar surfaces. These results were consistent with those reported by Ren et al. (2018a), who found that the biochar surface C content decreased and O content increased after two years in soil. It is worth noting that, after chemical oxidation of both AB and MB, the decrease in biochar C content and increase in O content were greater than those caused by the other two treatments. This indicates that the addition of an oxidant greatly accelerates the biochar oxidation process, promotes the formation of oxygen-containing functional groups, and has a greater impact on the biochar adsorption capacity.

The pH data in our study indicated that the two original biochars were alkaline. After the three aging treatments, the pH values showed a downward trend, and after chemical oxidation treatment, the two biochars became acidic. We suggested that the main cause of this change in biochar pH was the oxidation reaction on the biochar surface, which led to the non-biochemical adsorption of O and moisture in the environmental medium on the biochar surface increased. This increased the acidity of the surface and led to a decrease in the pH of the biochar. Changes in the O:C atomic ratios determined by the elemental analysis and XPS surface elemental compositions also confirmed this, and the same pH changes have been reported in other studies (Fang et al.,

2014; Mukherjee et al., 2014; Zhao et al., 2015). Regarding changes in the acidity and alkalinity of the biochar after chemical oxidation, Huff and Lee (2016) used H_2O_2 to oxidize biochar and considered that the decrease in biochar was due to the increase in the content of acidic functional groups such as hydroxyl groups and carboxyl groups after oxidation. Our XPS data show that the content of hydroxyl and carboxyl functional groups increased after chemical oxidation, and the degree of increase was much higher than the other two treated biochars. Therefore, we suggest that the change of the two biochars from alkaline to acidic after chemical oxidation was due to the increase in the content of acidic oxygen-containing functional groups.

The biochar aging process can also lead to changes in functional groups, thereby affecting the biochar adsorption capacity (Cheng and Lehmann, 2009; Keiluweit et al., 2010). In our study, we used FTIR to study the changes in functional groups of the biochar samples and XPS to study the development of surface functional groups. To summarize: 1) The content of O-containing functional groups in the two biochars increased after all three treatments, except for FAB, as indicated by the XPS data. 2) The FTIR spectra showed that the transmittance of the hydroxyl peaks in the two biochars increased after aging treatment excepted FAB. However, 3) the transmittance of aromatic C—C, C═C, and C—H bond peaks decreased after aging treatments. Our results were consistent with those reported in previous studies (Yao et al., 2010; Lin et al., 2012; Pereira et al., 2014; Ghaffar et al., 2015), and the changes in functional groups were considered to be caused by oxidation (Mia et al., 2017a).

4.2. Changes in Pb adsorption properties of biochars before and after aging

Research on the biochar adsorption mechanism of heavy metals is of great significance for the promotion and application of biochar. In our isothermal adsorption experiments, as the initial Pb concentration of the solution increased, the amount of Pb adsorbed on all biochar samples tended to stabilize or grow slowly. This can be explained by the fact that when the initial concentration of the solution was low, the adsorbent could provide sufficient adsorption sites and active groups. However, as the initial concentration of the solution increased, the adsorption sites gradually became saturated, reactive groups would gradually decrease to an extent due to the effect of adsorption, and finally the adsorbent reached saturation adsorption. The Langmuir model is an ideal monolayer adsorption model that assumes all points have the same affinity for the adsorbate and adsorption occurs at one adsorption point. On the other hand, the Freundlich model is suitable for multilayer adsorption on non-uniform surfaces. Interestingly, the adsorption of Pb by AB and MB were better fitted by the Langmuir model, whereas those of FAB, DAB, and DMB were better fitted by the Freundlich model. This indicated that the adsorption behaviors of AB and MB after chemical oxidation and of MB after freeze-thaw cycles did not change, and the adsorption process was approximately monolayer adsorption. In contrast, the adsorption behaviors of AB and MB after dry-wet cycles and AB after freeze-thaw cycles changed to multi-layer adsorption. In addition, our kinetic adsorption experiments showed that the adsorption of Pb with all biochar samples was better fitted by the pseudo-second-order kinetic model, showing that the Pb adsorption properties of the two biochars did not change after aging, which was a complex process containing both physical and chemical reactions (Ho and McKay, 1999; Fan et al., 2018b).

From our experimental results, the amount of O-containing functional groups in both biochars increased after chemical oxidation, and carboxyl groups were detected in CMB. This may be one of the reasons for the increase in maximum adsorption capacity in the Langmuir model, as an increase in O-containing functional groups can provide more adsorption sites for Pb adsorption, thereby increasing the Pb adsorption capacity by the complexation of surface free carboxyl and hydroxyl functional groups with Pb (Lu et al., 2012; Yang et al., 2014). In addition, metal precipitation cannot be ignored during the sorption process (Cao et al., 2009; Lu et al., 2012). Kołodyńska et al. (2012) reported that in the pH range 1.0 to 5.5, almost 100% of Pb is present in the Pb(II) form. When the pH exceeds this range, Pb will precipitate as $Pb(OH)_2$ in the solution. To study whether Pb precipitated in our research, we monitored the change in pH during kinetic adsorption. As shown in Fig. S2, in AB and its three treated biochars, except for CAB, the pH was maintained between 4.7 and 4.8 after 60 min, and the pH of AB, FAB, and GAB during adsorption was between 5.2 and 5.8. Similarly, in MB and its three treated biochars, except for CMB, the pH was maintained between 3.25 and 3.5 during adsorption, and the pH of AB, FAB, and GAB during adsorption was between 5.25 and 6.0. For the adsorption of Pb, both Zhang et al. (2018) and Liu et al. (2019) used pH conditions of 6.0. Therefore, we considered that the adsorption of Pb in our experiments also contained a small amount of precipitation.

In addition, increased SSA will increase the maximum adsorption capacity by enhancing the contact area. The SSAs of AB and MB increased by 19.19% and 17.24% after chemical oxidation, respectively. Furthermore, after MB was treated with freeze-thaw cycles, its SSAs showed downward trends. Thus, although O-containing functional group contents of FMB increased, the maximum adsorption capacities decreased. Therefore, we suggested that the adsorption of Pb by FMB was mainly physical adsorption arising from van der Waals forces between the adsorbate and adsorbent. Here, the decrease in SSA had a greater influence on the maximum adsorption capacity, as a smaller SSA provides fewer binding sites. Moreover, changes in the isothermal adsorption behavior of AB after freeze-thaw cycles, dry-wet cycles, and MB after dry-wet cycles indicate that the adsorption process changed from monolayer adsorption to multi-layer adsorption. Chemical adsorption is monolayer adsorption and physical adsorption can be either monolayer or multilayer adsorption. Our adsorption kinetic experiments show that adsorption is a complex process containing both physical and chemical reactions. Therefore, we suggested that the effect of physical adsorption lead to changes in adsorption behavior. Our SSA data also support this, which show decreases in the SSA of FAB, DAB, and DMB.

5. Conclusion

The aging of biochar changes its physicochemical properties and affects its Pb adsorption behavior, and these changes differ for different types of biochar. The SSAs of the two different biochars increase after chemical oxidation and decrease after freeze-thaw cycles and dry-wet cycles. Changes in SSA affect the number of binding sites, thereby affecting the Pb adsorption capacity of biochar arising from van der Waals forces between the adsorbent and adsorbate. The content of O-containing functional groups on the surfaces of the two different biochars increases after treatment, except for FAB. An increase in O-containing functional group content enhances the Pb adsorption capacity of biochar via complexation of carboxyl and hydroxyl functional groups with Pb, and other mechanisms. In our study, the Pb adsorption capacity of all the biochar samples was due to the complexation of surface free carboxyl and hydroxyl functional groups with Pb and van der Waals forces between the adsorbate and adsorbent greatly. Limited metal precipitation also occurred during the adsorption process. Our research in this area will offer insights regarding the implications of biochar aging on contaminant behavior.

Declaration of Competing Interest

The authors declare that they have no known competing financial interests or personal relationships that could have appeared to influence the work reported in this paper.

Acknowledgments

We thank Professor Hui Shi at the Xi'a University of Architecture and Technology for his assistance with the sample analyses. We also

acknowledge funding from the National Key Research and Development Plan of China (2016YFC0501702, 2017YFC0504504), the National Natural Science Foundation of China (41571225), and the STS project of the Chinese Academy of Sciences (KFJ-STS-ZDTP-012).

Appendix A. Supplementary data

Supplementary data to this article can be found online at https://doi.org/10.1016/j.scitotenv.2019.134223.

References

Ahmad, M., Rajapaksha, A.U., Lim, J.E., Zhang, M., Bolan, N., Mohan, D., et al., 2014. Biochar as a sorbent for contaminant management in soil and water: a review. Chemosphere 99 (3), 19–33.

Beesley, L., Marmiroli, M., 2011. The immobilisation and retention of soluble arsenic, cadmium and zinc by biochar. Environ. Pollut. 159 (2), 474–480.

Brunauer, S., Emmett, P.H., Teller, E., 1938. J. Am. Chem. Soc. 60, 309.

Cao, X., Ma, L., Gao, B., Harris, W., 2009. Dairy-manure derived biochar effectively sorbs lead and atrazine. Environ. Sci. Technol. 43 (9), 3285–3291.

Chen, B., Yuan, M., 2011. Enhanced sorption of polycyclic aromatic hydrocarbons by soil amended with biochar. J. Soils Sediments 11 (1), 62–71.

Cheng, C.H., Lehmann, J., 2009. Ageing of black carbon along a temperature gradient. Chemosphere 75 (8), 0–1027.

Cheng, C.H., Lehmann, J., Thies, J.E., Burton, S.D., Engelhard, M.H., 2006. Oxidation of black carbon by biotic and abiotic processes. Org. Geochem. 37, 1477–1488.

Demirbas, A., 2004. Effects of temperature and particle size on bio-char yield from pyrolysis of agricultural residues. J. Anal. Appl. Pyrol. 72 (2), 243–248.

Fan, Q., Cui, L., Quan, G., Wang, S., Sun, J., Han, X., et al., 2018a. Effects of wet oxidation process on biochar surface in acid and alkaline soil environments. Materials 11 (12), 2362.

Fan, Q., Sun, J., Chu, L., Cui, L., Quan, G., Yan, J., et al., 2018b. Effects of chemical oxidation on surface oxygen-containing functional groups and adsorption behavior of biochar. Chemosphere 207, 33–40.

Fang, Q., Chen, B., Lin, Y., Guan, Y., 2014. Aromatic and hydrophobic surfaces of wood-derived biochar enhance perchlorate adsorption via hydrogen bonding to oxygen-containing organic groups. Environ. Sci. Technol. 48 (1), 279–288.

Freundlich, H.M.F., 1906. Adsorption in solution. Z. Phys. Chem. 57, 385–470.

Ghaffar, A., Ghosh, S., Li, F., Dong, X., Zhang, D., Wu, M., et al., 2015. Effect of biochar aging on surface characteristics and adsorption behavior of dialkyl phthalates. Environ. Pollut. 206, 502–509.

Guo, G., Zhou, Q., Ma, L.Q., 2006. Availability and assessment of fixing additives for the in situ remediation of heavy metal contaminated soils: a review. Environ. Monit. Assess. 116 (1–3), 513–528.

Guo, Y., Tang, W., Wu, J., Huang, J., Dai, J., 2014. Mechanism of Cu (II) adsorption inhibition on biochar by its aging process. J. Environ. Sci. 26 (10), 2123–2130.

Hale, S.E., Hanley, K., Lehmann, J., Zimmerman, A.R., Cornelissen, G., 2011. Effects of chemical, biological, and physical aging as well as soil addition on the sorption of pyrene to activated carbon and biochar. Environ. Sci. Technol. 45, 10445–10453.

Heitkötter, J., Marschner, B., 2015. Interactive effects of biochar ageing in soils related to feedstock, pyrolysis temperature, and historic charcoal production. Geoderma 245, 56–64.

Herath, H.M.S.K., Camps-Arbestain, M., Hedley, M., 2013. Effect of biochar on soil physical properties in two contrasting soils: an Alfisol and an Andisol. Geoderma 209, 188–197.

Ho, Y.S., McKay, G., 1999. Pseudo-second order model for sorption processes. Process Biochem. 34, 451–465.

Huff, M.D., Lee, J.W., 2016. Biochar-surface oxygenation with hydrogen peroxide. J. Environ. Manag. 165, 17–21.

Keiluweit, M., Nico, P.S., Johnson, M.G., Kleber, M., 2010. Dynamic molecular structure of plant biomass-derived black carbon (biochar). Environ. Sci. Technol. 44 (4), 1247–1253.

Kołodyńska, D., Wne˛trzak, R., Leahy, J.J., Hayes, M.H.B., Kwapiński, W., Hubicki, Z., 2012. Kinetic and adsorptive characterization of biochar in metal ions removal. Chem. Eng. J. 197, 295–305.

Langmuir, I., 1916. The constitution and fundamental properties of solids and liquids. I. Solids. J. Am. Chem. Soc. 38, 2221–2295.

Lehmann, J., Gaunt, J., Rondon, M., 2006. Bio-char sequestration in terrestrial ecosystems - a review. Mitig. Adapt. Strat. GL. 11 (2), 403–427.

Lehmann, J., Skjemstad, J., Sohi, S., Carter, J., Barson, M., Falloon, P., Coleman, K., Woodbury, P., Krull, E., 2008. Australian climate|[ndash]|carbon cycle feedback reduced by soil black carbon. Nat. Geosci. 1 (12), 832–835.

Li, H., Ye, X., Geng, Z., Zhou, H., Guo, X., Zhang, Y., Zhao, H., Wang, G., 2016. The influence of biochar type on long-term stabilization for Cd and Cu in contaminated paddy soils. J. Hazard. Mater. 304, 40–48.

Lin, Y., Munroe, P., Joseph, S., Kimber, S., Zwieten, L., 2012. Nanoscale organo-mineral reactions of biochars in ferrosol: an investigation using microscopy. Plant Soil 357, 369–380.

Liu, Z., Demisie, W., Zhang, M., 2013. Simulated degradation of biochar and its potential environmental implications. Environ. Pollut. 179, 146–152.

Liu, Z., Chen, X., Jing, Y., Li, Q., Zhang, J., Huang, Q., 2014. Effects of biochar amendment on rapeseed and sweet potato yields and water stable aggregate in upland red soil. Catena 123, 45–51.

Liu, X.J., Lai, D.G., Wang, Y., 2019. Performance of Pb(II) removal by an activated carbon supported nanoscale zero-valent iron composite at ultralow iron content. J. Hazard. Mater. 361, 37–48.

Lu, H., Zhang, W., Yang, Y., Huang, X., Wang, S., Qiu, R., 2012. Relative distribution of pb2+ sorption mechanisms by sludge-derived biochar. Water Res. 46 (3), 0–862.

Martin, S.M., Kookana, R.S., Zwieten, L.V., Krull, E., 2012. Marked changes in herbicide sorption-desorption upon ageing of biochars in soil. J. Hazard. Mater. 231, 70–78.

Mia, S., Dijkstra, F.A., Singh, B., 2017a. Chapter one - long-term aging of biochar: a molecular understanding with agricultural and environmental implications. Adv. Agron. 141, 1–51.

Mia, S., Dijkstra, F.A., Singh, B., 2017b. Aging induced changes in biochar's functionality and adsorption behavior for phosphate and ammonium. Environ. Sci. Technol. 51 (15), 8359–8367.

Mohan, D., Pittman, C.U., Bricka, M., et al., 2007. Sorption of arsenic, cadmium, and lead by chars produced from fast pyrolysis of wood and bark during bio-oil production. J. Colloid Interf. Sci. 310 (1), 57–73.

Mohan, D., Sarswat, Ankur, Ok, Yong Sik, Pittman Jr., Charles U., 2015. Organic and inorganic contaminants removal from water with biochar, a renewable, low cost and sustainable adsorbent, a critical review. Bioresour. Technol. 160 (5), 191–202.

Mukherjee, A., Zimmerman, A.R., Hamdan, R., Cooper, W.T., 2014. Physicochemical changes in pyrogenic organic matter (biochar) after 15 months of field aging. Solid Earth 5 (2), 693.

Park, J.H., Choppala, G.K., Bolan, N.S., Chung, J.W., Chuasavathi, T., 2011. Biochar reduces the bioavailability and phytotoxicity of heavy metals. Plant Soil 348 (1–2), 439–451.

Pereira, R.C., Camps Arbestain, M., Kaal, J., Vazquez Sueiro, M., Sevilla, M., Hindmarsh, J., 2014. Detailed carbon chemistry in charcoals from pre-European Maori gardens of New Zealand as a tool for understanding biochar stability in soils. Eur. J. Soil Sci. 65, 83–95.

Qian, L., Chen, M., Chen, B., 2015. Competitive adsorption of cadmium and aluminum onto fresh and oxidized biochars during aging processes. J. Soils Sediments 15 (5), 1130–1138.

Ren, X., Sun, H., Wang, F., Cao, F., 2016a. The changes in biochar properties and sorption capacities after being cultured with wheat for 3 months. Chemosphere 144, 2257–2263.

Ren, X., Yuan, X., Sun, H., 2016b. Dynamic changes in atrazine and phenanthrene sorption behaviors during the aging of biochar in soils. Environ. Sci. Pollut. R. 25 (1), 1–10.

Ren, X., Sun, H., Wang, F., Zhang, P., Zhu, H., 2018a. Effect of aging in field soil on biochar's properties and its sorption capacity. Environ. Pollut. 242, 1880–1886.

Ren, X., Wang, F., Zhang, P., Guo, J., Sun, H., 2018b. Aging effect of minerals on biochar properties and sorption capacities for atrazine and phenanthrene. Chemosphere 206, 51–58.

Singh, B.P., Cowie, A.L., 2014. Long-term influence of biochar on native organic carbon mineralisation in a low-carbon clayey soil. Sci. Rep. 4 (3), 3687.

Sorrenti, G., Masiello, C.A., Dugan, B., Toselli, M., 2016. Biochar physico-chemical properties as affected by environmental exposure. Sci. Total Environ. 563-564, 237–246.

Trigo, C., Spokas, K.A., Cox, L., Koskinen, W.C., 2014. Influence of soil biochar aging on sorption of the herbicides MCPA, nicosulfuron, terbuthylazine, indaziflam, and fluoroethyldiaminotriazine. J. Agric. Food Chem. 62 (45), 10855–10860.

Uchimiya, M., Lima, I.M., Thomas Klasson, K., Chang, S.C., Wartelle, L.H., Rodgers, J.E., 2010. Immobilization of heavy metal ions (cu^{ii}, cd^{ii}, ni^{ii}, and pb^{ii}) by broiler litter-derived biochars in water and soil. J. Agric. Food Chem. 58 (9), 5538–5544.

Wang, H., Feng, M., Zhou, F., Huang, X., Tsang, D.C.W., Zhang, W., 2017. Effects of atmospheric ageing under different temperatures on surface properties of sludge-derived biochar and metal/metalloid stabilization. Chemosphere 184, 176–184.

Wang, T., Stewart, C.E., Sun, C., Wang, Y., Zheng, J., 2018. Effects of biochar addition on evaporation in the five typical Loess Plateau soils. Catena 162, 29–39.

Xu, R.K., Zhao, A.Z., 2013. Effect of biochars on adsorption of Cu(II), Pb(II) and Cd(II) by three variable charge soils from southern China. Environ. Sci. Pollut. R. 20 (12), 8491–8501.

Yang, Y., Wei, Z., Zhang, X., Chen, X., Yue, D., Yin, Q., et al., 2014. Biochar from Alternanthera philoxeroides could remove Pb(II) efficiently. Bioresour. Technol. 171, 227–232.

Yao, F.X., Arbestain, M.C., Virgel, S., Blanco, F., Arostegui, J., Maciá-Agulló, J.A., et al., 2010. Simulated geochemical weathering of a mineral ash-rich biochar in a modified Soxhlet reactor. Chemosphere 80, 724–732.

Zama, E.F., Reid, B.J., Sun, G.X., Yuan, H.Y., Li, X.M., Zhu, Y.G., 2018. Silicon (Si) biochar for the mitigation of arsenic (As) bioaccumulation in spinach (Spinacia oleracean) and improvement in the plant growth. J. Clean. Prod. 189, 386–395.

Zhang, X., Wang, H., He, L., Lu, K., Sarmah, A., Li, J., Bolan, N.S., Pei, J., Huang, H., 2013. Using biochar for remediation of soils contaminated with heavy metals and organic pollutants. Environ. Sci. Pollut. R 20 (12), 8472–8483.

Zhang, Y., Cao, B., Zhao, L.L., Sun, L.L., Gao, Y., Li, J.J., Yang, F., 2018. Biochar-supported reduced graphene oxide composite for adsorption and coadsorption of atrazine and lead ions. Appl. Surf. Sci. 427, 147–155.

Zhao, Y., Zhang, B., Zhang, X., Wang, J., Liu, J., Chen, R., 2010. Preparation of highly ordered cubic naa zeolite from halloysite mineral for adsorption of ammonium ions. J. Hazard. Mater. 178 (1–3), 658–664.

Zhao, R., Coles, N., Wu, J., 2015. Carbon mineralization following additions of fresh and aged biochar to an infertile soil. Catena 125, 183–189.